JOURNAL OF COMPUTATIONAL PHYSICS 106, 319–336 (1993)

A Numerical Algorithm for Hydrodynamic Free Boundary Problems

WILLIAM G. SZYMCZAK* †

Information and Mathematical Sciences Branch - Code R44, Naval Surface Warfare Center, Silver Spring, Maryland 20903-5000

JOEL C. W. ROGERS‡

Department of Mathematics, Polytechnic University, Brooklyn, New York 11201-2907

AND

JAY M. SOLOMON† AND ALAN E. BERGER†

Information and Mathematical Sciences Branch - Code R44, Naval Surface Warfare Center, Silver Spring, Maryland 20903-5000

Received March 5, 1991; revised July 23, 1992

A generalized formulation of inviscid incompressible hydrodynamics as a system of conservation laws subject to a one-sided density constraint is used as the basis of a numerical algorithm for a variety of hydrodynamic free surface problems. Benchmark calculations for colliding masses of fluid and for the motion of a spherically symmetric bubble are compared with theoretical predictions. Also shown are profiles calculated for an evolving underwater bubble near a wall. Energy dissipation is introduced as a measure of turbulence and is used in analyzing the numerical results. Convergence behavior of the numerical algorithm is discussed. © 1993 Academic Press, Inc.

1. INTRODUCTION

The most familiar phenomenon associated with the motion of water with a free surface is probably the formation of waves. Almost as familiar is the breaking of waves. This latter phenomenon reflects a breakdown of the classical hydrodynamic theory, which presumes a one-to-one mapping of initial particle positions to their locations at a later time. We may generically ascribe the cause of such types of breakdown to "Helmholtz instability," which we equate with a loss of Lipschitz continuity (with respect to space) of the velocity field, since particle paths will never run together when the velocity field is Lipschitz continuous. Local existence in time of smooth solutions of hydrodynamic free boundary problems can be shown in special cases [1], but in general such existence is not to be expected. It is shown in [2] that, in the case of inviscid incompressible flows in the absence of surface tension, if a wave on any scale breaks at any time, then waves on smaller scales can break in arbitrarily short times. This calls into question the utility of the classical formulation of free-surface hydrodynamics for the treatment of any but a few special types of flows.

For this reason, a generalized formulation of inviscid incompressible hydrodynamics has been developed [2, 3], which reverts to the classical theory for smooth flows (the regime in which the classical theory applies). This generalized formulation is natural for the treatment of flows with complicated free boundaries, as it is topology-independent, in the sense that explicit tracking of the position of the fluid surface is not required by the solution algorithm. The salient feature of the generalized hydrodynamics is that the equations of motion are given in "conservation" form in a fixed domain, which may be $\mathscr{R}^N$ and that they are solved subject to a one-sided constraint on the mass density. The generalized treatment admits the possibility of flows in which there is a "spray" region, where the mass density is below that of the fluid, and also the possibility of energy loss in the flow due to collisions of fluid particles. This generalized formulation is reviewed in Section 2.

The purpose of the present paper is to give an efficient numerical method based on the generalized inviscid hydrodynamics of Refs. [2, 3]. A preliminary version of the current paper appeared in [4]. Since the present numerical method retains the features of the generalized formulation, it is well suited for treating problems where complex free surfaces are present and where collisions of fluid elements

* To whom correspondence should be addressed.

† Research supported by the Office of Naval Research under Contract N0001489WX24070, and by the Naval Surface Warfare Center Independent Research Fund.

‡ Research supported by the Navy–ASEE Summer Faculty Fellowship Program (1988–1990).

0021-9991/93 $5.00

Copyright © 1993 by Academic Press, Inc.
All rights of reproduction in any form reserved.

occur. As previously indicated, such difficulties often arise in the long time motion of incompressible, inviscid free surface problems.

Existing numerical methods using integral representations for potential flow (boundary integral or panel methods) have been successfully applied to classical problems (see, e.g., [5–8]). These methods require the explicit calculation of the location of the free surfaces, and they break down when collisions of fluid elements occur (as in the case of breaking surface waves). There has been recent progress in extending these procedures to treat the special case of an underwater bubble undergoing a change in topology from a sphere to a torus. This has been done in [7] by introducing and explicitly tracking a branch cut in the flow field and in [5] by adding a circulation to the flow field which balances the jump in potential across the cut. However, these procedures are still being validated and, as yet, have no straightforward extensions to either more general collisions (e.g., breaking waves) or three-dimensional problems.

Finite difference methods based on the incompressible equations have also been developed for free surface problems. The more robust of the existing methods use either a marker and cell (MAC) procedure (see, e.g., [9]) or a volume of fluid (VOF) variable (see, e.g., [10]) to follow the evolution of the incompressible fluid regions and delineate their free surface boundaries in a fixed computational mesh. In the MAC procedure, massless marker particles are dispersed in the fluid region and convected by the flow in a Lagrangian manner. Disadvantages of this approach include the additional storage required for locating the marker particles, and the additional logic required to locate the cells containing the free surfaces. In methods using a VOF variable, an auxiliary scalar field representing the volume of incompressible fluid per unit volume, is introduced and advanced in time using an equation expressing the conservation of incompressible fluid volume. The free surfaces are located at the discontinuities of the VOF variable. When collisions of fluid elements occur, these methods apparently rely on the physically unrealistic dissipation inherent in their differencing schemes to handle the resulting loss of flow smoothness. For example, whenever the VOF variable attains a value greater than one, the excess is simply ignored. While this approach may be adequate when the excesses are due to numerical truncation error, large errors may arise when fluid collisions occur.

In the present fixed domain method, the constrained mass density serves as a VOF variable. However, unlike the VOF approach, global conservation of mass and momentum is imposed. In the present method, the free surfaces appear naturally as slightly "smeared" interfaces which, in some respects, resembles the way shock waves are "captured" by many Eulerian, compressible flow codes. Another important feature of the present method is the physical model employed for the redistribution of mass and momentum resulting from collisions of fluid elements. Among other things, this treatment ensures that the global energy behaves in a manner similar to the global Lax entropy in compressible gas dynamics in that it cannot increase, and it may decrease, depending on the dynamics of the flow. Energy conservation occurs only in the special case of classical flows, where no collisions of fluid elements can take place.

Compressible flow codes have also been applied to free surface problems for "nearly" incompressible fluids; see, e.g., [11, 12]. These methods, however, are not particularly well suited for treating the *long time* motion of nearly incompressible fluids like water. In addition to the difficulties of specifying an appropriate equation of state for the nearly incompressible fluid, these methods require very small time steps for stability due to the very large acoustical speed in the fluid. The small time steps of the compressible codes near the incompressible limit restrict their usefulness for predicting the relatively long time motions of essentially incompressible fluids addressed by the present method.

The numerical algorithm is described here in the context of axially symmetric problems (see Section 3). As will be apparent from Section 3, that there is no conceptual change in extending the algorithm to three space dimensions, beyond the obvious larger scale of carrying out various numerical procedures in a region in $\mathscr{R}^3$ instead of $\mathscr{R}^+ \times \mathscr{R}$. To test the applicability of the method, two benchmark problems are considered (see Section 4). One is the model problem of the face-on collision of two cylindrical masses of liquid. The computed energy loss in this collision problem is seen to compare favorably with the analytical expression for the energy loss. The other is the periodic motion of a spherically symmetric underwater bubble in an "infinite" medium, for which there is a known analytical solution, see, e.g., [13]. In addition, computational results will be given for the motion of an underwater bubble near a solid bottom wall. In the latter problem, the collapse of an initially spherical bubble forms a reentrant water jet passing through the bubble's interior from top to bottom and impacting on the opposite side. After the jet breaks through the opposite side, the bubble becomes toroidal in shape. This agrees qualitatively with experimental observations.

2. GENERALIZED HYDRODYNAMICS

Here we shall summarize the equations that govern the evolution of the flow, with our primary aim being a concise description of the basis of the procedure used to obtain the numerical results described in Section 4. Consider a spatial domain, Ω, fixed for all time, which contains an incompressible fluid with mass density ρ_0. In this fixed domain,

the mass and momentum densities (ρ and $\rho\mathbf{u}$, respectively) are governed by conservation laws subject to the constraint

$$\rho \leqslant \rho_0. \tag{2.1}$$

The time varying *liquid* region is defined by

$$\mathscr{D}(t) = \{\mathbf{x} \in \Omega : \rho(\mathbf{x}, t) = \rho_0\}$$

and is determined by the solution. For reasons which will be apparent later in this description, the pressure P will be regarded as a dependent variable only in $\mathscr{D}(t)$. In any connected non-liquid portion of Ω, where $\rho < \rho_0$, the pressure is assumed to be constant (in space). Since surface tension effects will be neglected, we also assume that P is continuous.

Our procedure will carry us from a known description of the flow at a given time $t = t^n$ to a description of the flow at a later time $t^n + \tau$. The positive quantity τ is the *time step* and we may regard our treatment formally as generating an approximate flow which is meant to converge to an exact flow as $\tau \to 0$, in a nonlinear semigroup sense. The governing equations and the constraint are treated using a time split approach which approximates their solution at the new time step in distinct stages.

In the first stage of the algorithm, the advection of the flow under the influence of gravity is considered without regard to the constraint (2.1). The equations governing this stage are given by

$$\rho_t + \nabla \cdot (\rho \mathbf{u}) = 0, \tag{2.2}$$

$$(\rho \mathbf{u})_t + \nabla \cdot (\rho \mathbf{u}\mathbf{u}) = -\rho g \mathbf{k}, \tag{2.3}$$

where g is the gravitational constant and $-\mathbf{k}$ is the unit vector in the direction of the gravitational force. The initial values for the above are the known values ρ^n and $\mathbf{u}^n$ of the density and velocity at $t = t^n$. The solutions of (2.2), (2.3) at $t = t^n + \tau$ will be denoted by $\tilde{\rho}$, $\tilde{\mathbf{u}}$.

Solutions of (2.2) and (2.3) may generally be multiple-valued when fluid particles which have come from different locations arrive at the same point and thus collide. Weak solutions which are single-valued in their dependence on the Eulerian coordinates can be constructed in a multitude of ways, and in order to prescribe a particular single-valued solution we have to insert a selection rule from physics, in addition to the requirement that mass and momenta be conserved in collisions. In the present version of generalized hydrodynamics, we do so by requiring that all collisions of fluid particles be *inelastic*. Such inelastic solutions can be represented using a Boltzmann-type approach (see [2]). A consequence of this representation is that the energy, defined by

$$e(\rho, \mathbf{u}) = \int_\Omega (\tfrac{1}{2}\rho \mathbf{u}^2 + \rho g z)\, d\mathbf{x},$$

where $\mathbf{u}^2 = \mathbf{u} \cdot \mathbf{u}$ and z is the coordinate in the direction of $\mathbf{k}$, satisfies

$$e(\tilde{\rho}, \tilde{\mathbf{u}}) - e(\rho^n, \mathbf{u}^n) = -\tau \Phi_1 \qquad \text{with} \quad \Phi_1 \geqslant 0 \tag{2.4}$$

when the fluxes across the boundaries of Ω are neglected. Further, if no collisions take place during the time step then $\Phi_1 = 0$.

For numerical efficiency, the "inelastic solution" of (2.2), (2.3) is approximated in the present work using an explicit finite difference scheme rather than a Boltzmann approach. This difference scheme is based on the integral form of (2.2), (2.3) on a computational cell with the time averaged convective fluxes across the cell faces chosen to model the inelastic solution. Details of this scheme, along with the associated explicit stability condition on τ, will be described in Section 3.

In the remaining stages of the algorithm, the provisional values of mass and momentum densities, $\tilde{\rho}$ and $\tilde{\rho}\tilde{\mathbf{u}}$, are corrected so that the constraint (2.1) is satisfied. One may imagine that, while the flow is convecting according to (2.2) and (2.3), an extremely rapid diffusion of excess mass is taking place wherever (2.1) is violated. The motion associated with this diffusion of mass also has to affect the momentum. The rapid diffusion of excess mass is governed by the equation

$$\theta_{t^*} = \Delta f(\theta), \tag{2.5a}$$

where $\Delta = \nabla \cdot \nabla$,

$$f(\theta) = \begin{cases} \theta - \rho_0 & \text{if} \quad \theta - \rho_0 > 0, \\ 0 & \text{otherwise,} \end{cases} \tag{2.5b}$$

$t^* \equiv \alpha t$, α is the diffusion coefficient, and θ is an instantaneous mass density satisfying the initial condition

$$\theta(0) = \tilde{\rho}. \tag{2.5c}$$

We are interested in (2.5) when $\alpha \to \infty$. Hence, after a time τ, $t^* = \alpha\tau \to \infty$, and we have the corrected mass density

$$\bar{\rho} = \lim_{t^* \to \infty} \theta(t^*). \tag{2.6}$$

The problem (2.5) is a one-phase Stefan problem and it follows that $\bar{\rho}$ given by (2.6) satisfies the constraint (2.1). The associated modified momentum density $\bar{\rho}\bar{\mathbf{u}}$ is given by (cf. [2])

$$\bar{\rho}\bar{\mathbf{u}} = \tilde{\rho}\tilde{\mathbf{u}} + \Delta(\tilde{\mathbf{u}}H) - \frac{2}{\tau}\nabla H, \tag{2.7a}$$

where

$$H = \int_0^\infty f(\theta(t^*))\, dt^*. \tag{2.7b}$$

Instead of solving the Stefan problem (2.5) to steady state, H and $\bar{\rho}$ can be found more efficiently [14] by solving the "obstacle" problem: find $H \geqslant 0$ such that

$$\Delta H = \bar{\rho} - \tilde{\rho} = \begin{cases} \rho_0 - \tilde{\rho} & \text{if } H > 0, \\ 0 & \text{if } H = 0. \end{cases} \tag{2.8}$$

Then $\bar{\rho}$ is simply ρ_0 in the support of H and $\tilde{\rho}$ elsewhere.

It has been shown in [2] that $\bar{\rho}$, $\bar{\mathbf{u}}$ represent a consistent approximation to the solution of classical free surface problems, where the velocity field is smoothly differentiable in the incompressible liquid region and the pressure is zero in the non-liquid region. For such classical problems, it follows from (2.7a) and (2.3) that $2H/\tau^2$ takes the part of the pressure in more usual formulations of hydrodynamics and thus H is $O(\tau^2)$. Unfortunately, the use of (2.7a) may, in certain circumstances, lead to spurious energy sources in the approximate solution. This difficulty can be eliminated by refining the treatment of the density constraint (2.1) as indicated in [3]. The method of [3] has the additional advantage that it is directly applicable to problems where non-zero pressures are specified in the non-liquid regions.

Following [3], the constraint (2.1) is required to be satisfied, not only at the particular discrete time steps, but also in a "strip" [15] at each of these times, in the sense that

$$\frac{d\rho}{dt} = \rho_t + \mathbf{u} \cdot \nabla \rho \leqslant 0 \qquad \text{when} \quad \rho = \rho_0, \tag{2.9}$$

at each of the discrete times. In view of (2.2), (2.9) becomes

$$\nabla \cdot \mathbf{u} \geqslant 0 \qquad \text{when} \quad \rho = \rho_0. \tag{2.10}$$

Both (2.1) and (2.10) are imposed at each time step. The constraint (2.10) is satisfied using a Lagrange multiplier P (the pressure) whose gradient appears in the momentum equation. This procedure is similar to that commonly used in incompressible hydrodynamics. In the present context, however, the momentum equations are considered on the entire fixed domain while the constraint (2.10) is active (and thus the pressure is a dependent variable) only in the liquid sub-region where $\rho = \rho_0$. In the algorithm, H and $\bar{\rho}$ (the final density for the new time step) are still determined using (2.8). The final velocity at the new time step, $\mathbf{u}^*$, is obtained by dividing (2.7a) into two stages. Accordingly, we first define $\bar{\mathbf{u}}$ using

$$\bar{\rho}\bar{\mathbf{u}} = \tilde{\rho}\tilde{\mathbf{u}} + \Delta(\bar{\mathbf{u}}H), \tag{2.11}$$

and then obtain $\mathbf{u}^*$ from

$$\bar{\rho}\mathbf{u}^* = \begin{cases} \bar{\rho}\bar{\mathbf{u}} - \nabla(P\tau) & \text{where } \bar{\rho} = \rho_0, \\ \bar{\rho}\bar{\mathbf{u}} & \text{elsewhere.} \end{cases} \tag{2.12}$$

The pressure P is determined in the liquid domain $\mathscr{D} = \{\mathbf{x} : \bar{\rho} = \rho_0\}$, subject to the constraint $P \geqslant P_C$, where P_C is the cavitation pressure of the liquid. This leads to the obstacle problem on $\mathscr{D}$: find $P \geqslant P_C$ such that

$$\Delta(P\tau) = \begin{cases} \bar{\rho}\nabla \cdot \bar{\mathbf{u}} & \text{if } P > P_C, \\ 0 & \text{if } P = P_C. \end{cases} \tag{2.13}$$

Recall that in the non-liquid portions of the fixed domain, where $\bar{\rho} < \rho_0$, P is specified. In the subset $\mathscr{D}^* \subset \mathscr{D}$, where $\bar{\rho} = \rho_0$ and $P > P_C$, (2.12) is a decomposition of the vector $\bar{\mathbf{u}}$ into a divergence-free component, $\mathbf{u}^*$, and an irrotational component, $\nabla(P\tau)/\rho_0$. Thus $\mathscr{D}^*$ represents the *incompressible liquid region.* In the regions where $\bar{\rho} = \rho_0$ and $P = P_C$, $\nabla \cdot \mathbf{u}^* = \nabla \cdot \bar{\mathbf{u}} \geqslant 0$ and it follows that the density is non-increasing with time. Hence there is the possibility of cavitation of the liquid as indicated by the appearance of non-liquid regions, where $P = P_C$ in the solution.

In summary, the algorithm for the full time step is given by the three-stage procedure

$$(\rho^n, \mathbf{u}^n) \to (\tilde{\rho}, \tilde{\mathbf{u}}) \to (\bar{\rho}, \bar{\mathbf{u}}) \to (\bar{\rho}, \mathbf{u}^*) \equiv (\rho^{n+1}, \mathbf{u}^{n+1}).$$

Formally, we can analyze the change in energy associated with one full step of the algorithm. We note from (2.11) and (2.8) that

$$\bar{\rho}\bar{\mathbf{u}}^2 - \tilde{\rho}\tilde{\mathbf{u}}^2 = -\tilde{\rho}(\bar{\mathbf{u}} - \tilde{\mathbf{u}})^2 + \Delta(H\bar{\mathbf{u}}^2) - 2H(\nabla\bar{\mathbf{u}})^2$$

and

$$\bar{\rho}gz - \tilde{\rho}gz = \Delta(gzH) - 2\nabla \cdot (gH\mathbf{k}).$$

Thus, neglecting fluxes across the boundaries of Ω, one has

$$\begin{aligned} e(\bar{\rho}, \bar{\mathbf{u}}) - e(\tilde{\rho}, \tilde{\mathbf{u}}) &= -\int_\Omega (\tilde{\rho}(\bar{\mathbf{u}} - \tilde{\mathbf{u}})^2/2 + H(\nabla\bar{\mathbf{u}})^2) \\ &\equiv -\tau\Phi_2. \end{aligned} \tag{2.14}$$

Further, if $\mathscr{D}^*$ has a piecewise regular boundary, we have from (2.12) that

$$\begin{aligned} e(\bar{\rho}, \mathbf{u}^*) - e(\bar{\rho}, \bar{\mathbf{u}}) + \tau \int_{\partial\mathscr{D}^*} (\mathbf{u}^* \cdot \mathbf{n})P \\ = -\frac{\tau^2}{2}\int_{\mathscr{D}^*} (\nabla P)^2/\bar{\rho} \equiv -\tau\Phi_3, \end{aligned} \tag{2.15}$$

where $\partial\mathscr{D}^*$ is the boundary of $\mathscr{D}^*$ and $\mathbf{n}$ is its unit outer normal. The last term on the left-hand side of (2.15) represents the work done by the boundaries of the incompressible liquid during the time step. It follows from (2.4), (2.14), and (2.15) that

$$e(\bar{\rho}, \mathbf{u}^*) - e(\rho^n, \mathbf{u}^n) + \tau \int_{\partial\mathscr{D}^*} (\mathbf{u}^* \cdot \mathbf{n}) P = -\tau\Phi, \quad (2.16)$$

where $\Phi = \Phi_1 + \Phi_2 + \Phi_3 \geq 0$. Thus, neglecting fluxes across $\partial\Omega$, the sum of the energy and the boundary work cannot increase (and may decrease) regardless of the size of the time step τ. For classical flows, the regularity of the velocity field does not allow collisions of the fluid elements and the dissipation Φ will vanish as $\tau \to 0$. (For such flows the conservation of energy (i.e., (2.16) with $\Phi = 0$) is a consequence of the conservation of mass and momentum.) For the generalized flows considered here, the velocity fields may not have the required regularity and inelastic collisions of the fluid elements can take place with an associated loss of energy. In such non-classical problems, the portion of the energy dissipation which does not vanish as $\tau \to 0$ is an intrinsic property of the flow and may be attributed to turbulence. For a discussion of the connection between stability, turbulence, and energy dissipation in the generalized hydrodynamics, the reader is referred to [16].

Underwater bubbles. To illustrate the application of the above algorithm, we consider the evolution of an underwater bubble. In this problem, the bubble is modeled as a uniform pressure region $\mathscr{B}$ with pressure P_B given by the adiabatic gas law:

$$P_B V_B^{\gamma} = \text{const}, \quad (2.17)$$

where γ is the ratio of the specific heats and V_B is the volume of the bubble. Above the water there is the atmospheric region $\mathscr{A}$ which has a constant pressure P_A. If the obstacle in (2.13) is active such that $\nabla \cdot \mathbf{u} > 0$ in some region for a finite length of time, then a third non-water region ($\bar{\rho} < \rho_0$) will evolve. This region will be referred to as the cavitation region $\mathscr{C}$ and will have constant pressure P_C. In the absence of viscosity and surface tension the cavitation pressure is the saturation vapor pressure of the liquid. We are assuming $P_A \geq P_C$ and $P_B \geq P_C$. The regions $\mathscr{A}$, $\mathscr{B}$, and $\mathscr{C}$ can vary with time, depending on the density field. Since the density at the new time is determined in the second stage of the algorithm, these regions are updated before performing the final stage of the algorithm. A procedure for determining these regions for the fully discretized problem is given in the next section.

For the last stage of the algorithm, the pressure in the non-water regions (where $\bar{\rho} < \rho_0$) is given by

$$P = \begin{cases} P_A & \text{if } \mathbf{x} \in \mathscr{A}, \\ P_B & \text{if } \mathbf{x} \in \mathscr{B}, \\ P_C & \text{if } \mathbf{x} \in \mathscr{C}, \end{cases} \quad (2.18)$$

while the pressure in the water region (where $\bar{\rho} = \rho_0$) is determined by solving the obstacle problem (2.13). Because the pressure is continuous in the entire fixed domain, (2.18) provides boundary values for (2.13) at the interfaces between the water and non-water regions. The solution of (2.13) can introduce yet another region $\mathscr{C}_0$, where $\bar{\rho} = \rho_0$ and $P = P_C$. The region $\mathscr{D}^*$, representing the incompressible water, is then the complement of the closure of $\mathscr{A} \cup \mathscr{B} \cup \mathscr{C} \cup \mathscr{C}_0$ in Ω.

In the idealized situation, where the interface boundaries between $\mathscr{D}^*$ and the regions $\mathscr{A}$, $\mathscr{B}$, $\mathscr{C}$, and $\mathscr{C}_0$ are piecewise smooth surfaces and the boundaries of Ω are sufficiently far from $\mathscr{B}$, $\mathscr{C}$, and $\mathscr{C}_0$ so that there are no fluxes across (and no work done at) the boundaries of Ω, the change in energy over a time step is given by (2.16) with the boundary work term determined by

$$\int_{\partial\mathscr{D}^*} (\mathbf{u}^* \cdot \mathbf{n}) P = \int_{\partial\mathscr{D}^*} (\mathbf{u}^* \cdot \mathbf{n})(P - P_C)$$
$$= -(P_B - P_C)\frac{dV_B}{dt} - (P_A - P_C)\frac{dV_A}{dt}, \quad (2.19)$$

where V_A is the volume of $A \cap \Omega$. In (2.19), the first equality follows from the fact that $\mathbf{u}^*$ is divergence-free in $\mathscr{D}^*$ and P_C is a constant. The second equality follows from the continuity of P and the fact that the interface boundaries, being free surfaces, propagate with speed $\mathbf{u}^* \cdot \mathbf{n}$ in the direction of $\mathbf{n}$. Thus,

$$\frac{dV_B}{dt} = -\int_{\partial B} \mathbf{u}^* \cdot \mathbf{n} \quad \text{and} \quad \frac{dV_A}{dt} = -\int_{\partial A \cap \partial\mathscr{D}^*} \mathbf{u}^* \cdot \mathbf{n}.$$

Formally taking the limit as $\tau \to 0$ in (2.16) and using (2.17) and (2.19), we obtain

$$\frac{dE}{dt} = -\lim_{\tau \to 0} \Phi, \quad (2.20a)$$

where E, the total energy for the underwater bubble problem, is defined by

$$E = e(\rho, \mathbf{u}) + \left(\frac{P_B}{\gamma - 1} + P_C\right) V_B - (P_A - P_C)\, V_A. \quad (2.20b)$$

In classical problems, where there are no fluid collisions, the right-hand side of (2.20a) is zero; whereas, in nonclassical cases the limit may not even exist in the usual sense.

3. THE NUMERICAL ALGORITHM

We consider an axisymmetric (r, z) coordinate system on which a tensor product grid with cell vertex points (r_i, z_j) with $0 = R_L = r_0 < r_1 < \cdots < r_N = R_R$, and $Z_B = z_0 < z_1 < \cdots < z_M = Z_T$, is defined. The cell $C_{i+1/2,j+1/2}$ centered at $(r_{i+1/2}, z_{j+1/2})$, where $r_{i+1/2} = (r_{i+1} + r_i)/2$, and $z_{j+1/2} = (z_{j+1} + z_j)/2$ has width $\Delta r_{i+1/2} = r_{i+1} - r_i$ and height $\Delta z_{j+1/2} = z_{j+1} - z_j$. Let Ω denote the fixed domain $(R_L, R_R) \times (Z_B, Z_T)$. On the boundaries of Ω, conditions are imposed to simulate the presence of a solid wall boundary Γ_w, or an infinite domain along a "cutoff" boundary Γ_c. Also let Γ_a denote the axis of symmetry $r = 0$, $Z_B \leqslant z \leqslant Z_T$.

The subscript h is used to denote spatial finite dimensional approximations. A staggered (density, velocity)-pressure grid system is employed with density ρ_h defined by its piecewise cell average values $\rho_{i+1/2,j+1/2}$. The velocity is represented by $\mathbf{u}_h^* = \mathbf{u}_h + \mathbf{u}_h^\perp$, where $\mathbf{u}_h$ is the cell average and $\int \mathbf{u}_h^\perp = 0$ on each cell. The "correction" $\mathbf{u}_h^\perp$ is used only in the last stage of the algorithm. The weighted mass density $m = r\rho$ is also defined at the cell centers, $m_{i+1/2,j+1/2} \equiv r_{i+1/2}\rho_{i+1/2,j+1/2}$. The discrete pressure P_h is a continuous piecewise bilinear function, with nodal values P_{ij} approximating the pressure at (r_i, z_j).

Following Section 2, the numerical algorithm advances the computed density, ρ_h, and velocity, $\mathbf{u}_h^*$, at a time t^n to a time $t^{n+1} = t^n + \tau^n$ using the following steps:

(1) Convection (cf. (2.2)–(2.3)),

$$(\rho_h^n, \mathbf{u}_h^n) \to (\tilde{\rho}_h, \tilde{\mathbf{u}}_h).$$

(2) Redistribution of density and momenta (cf. (2.8), (2.11)),

$$(\tilde{\rho}_h, \tilde{\mathbf{u}}_h) \to (\bar{\rho}_h, \bar{\mathbf{u}}_h).$$

(3) Pressure correction (cf. (2.12), (2.13), and (2.19)),

$$(\bar{\rho}_h, \bar{\mathbf{u}}_h + (\mathbf{u}_h^\perp)^n) \to (\bar{\rho}_h, (\mathbf{u}_h^*)^{n+1}) \equiv (\rho_h^{n+1}, \mathbf{u}_h^{n+1} + (\mathbf{u}_h^\perp)^{n+1}).$$

We remark that in the case of inviscid incompressible flow with no free surfaces and thus $\rho = \rho_0$ everywhere, the algorithm of Section 2 reduces to the second-order projection method of Bell *et al.* [17, 18]. Formal second-order accuracy is retained in the numerical algorithm by coupling the pressure gradient terms into the convection step. However, since free surfaces are initialized in our applications using discontinuous density and velocity fields, second-order accuracy cannot be expected in our numerical results.

Convection

For axisymmetric problems the unconstrained convection equations (2.2)–(2.3) have the form

$$\mathbf{U}_t + \mathbf{F}_r + \mathbf{G}_z = \mathbf{R}, \tag{3.1}$$

where

$$\mathbf{U} = \begin{pmatrix} mu \\ mv \\ m \end{pmatrix}, \qquad \mathbf{F} = u\mathbf{U} = \begin{pmatrix} mu^2 \\ muv \\ mu \end{pmatrix},$$

$$\mathbf{G} = v\mathbf{U} = \begin{pmatrix} muv \\ mv^2 \\ mv \end{pmatrix}, \qquad \mathbf{R} = \begin{pmatrix} 0 \\ -mg \\ 0 \end{pmatrix}.$$

In the above, u and v denote the r and z components of $\mathbf{u}$. These equations are discretized using a formally second-order Godunov-type method which uses slope limiting in space and explicit predictor–corrector time stepping. In particular the present scheme closely follows the development by Davis [19].

From the cell averaged values for the velocity $\mathbf{u}^n_{i+1/2,j+1/2}$ and weighted mass density $m^n_{i+1/2,j+1/2}$ at time t^n, slopes are computed in each coordinate direction using central differences with monotonicity constraints. For example, for the u velocity component, central, forward, and backward divided differences

$$u_r^c = \frac{u_{i+3/2} - u_{i-1/2}}{r_{i+3/2} - r_{i-1/2}}, \qquad u_r^f = \frac{u_{i+3/2} - u_{i+1/2}}{\Delta r_{i+1/2}},$$

$$u_r^b = \frac{u_{i+1/2} - u_{i-1/2}}{\Delta r_{i+1/2}}$$

are computed in the r direction. (Throughout this section, when there is no ambiguity, inactive indices are dropped for simplicity. For example, in the above, the j index and n superscript have been suppressed.) The central difference slope is limited using the formula

$$(u_r)_{i+1/2} = \begin{cases} \operatorname{sgn}(u_r^c)\min(|u_r^c|, 2|u_r^f|, 2|u_r^b|) & \text{if } u_r^f u_r^b > 0, \\ 0 & \text{if } u_r^f u_r^b < 0. \end{cases}$$

This prescription ensures discrete monotonicity in the sense that if $u_{i+3/2} \geqslant u_{i+1/2} \geqslant u_{i-1/2}$ then $u_{i+3/2} \geqslant u_{i+1/2} + (u_r)_{i+1/2}\Delta r_{i+1/2}/2 \geqslant u_{i+1/2} \geqslant u_{i+1/2} - (u_r)_{i+1/2}\Delta r_{i+1/2}/2 \geqslant u_{i-1/2}$. Slopes are determined at the boundary cells using extrapolated values for the velocity or density. For example, across the axisymmetric centerline or a solid wall boundary the normal velocity is extrapolated as an odd function. In all other cases the velocities and density are extrapolated with the same value as in the adjacent interior cell (which

effectively yields zero normal slopes). These monotonized slopes are used as difference approximations to the partial derivatives $\mathbf{u}_r^n$, $\mathbf{u}_z^n$, m_r^n, and m_z^n at the cell centers. Further remarks on slope limiting can be found in [17, 20].

Predicted velocity values $\mathbf{u}_{i+1/2,j+1/2}^{n+1/2}$, and mass density values $m_{i+1/2,j+1/2}^{n+1/2}$ at the half time step are computed using the first two terms in the Taylor series expansions in space and time. The time derivatives are expressed in terms of the spatial derivatives using (3.1) with the addition of the pressure gradient term indicated by (2.12). The spatial derivatives of $\mathbf{u}$ and m are approximated using the limited slopes. First the left, right, top, and bottom values (designated by superscripts L, R, T, B, respectively) within each cell are computed. For example, approximations to $\mathbf{u}$ at the right and left edges of cell $C_{i+1/2,j+1/2}$ are

$$\mathbf{u}_{i+1/2,j+1/2}^{n,R} = \mathbf{u}_{i+1/2,j+1/2}^{n} + \frac{\Delta r_{i+1/2}}{2}(\mathbf{u}_r)_{i+1/2,j+1/2}^{n}$$

and

$$\mathbf{u}_{i+1/2,j+1/2}^{n,L} = \mathbf{u}_{i+1/2,j+1/2}^{n} - \frac{\Delta r_{i+1/2}}{2}(\mathbf{u}_r)_{i+1/2,j+1/2}^{n},$$

respectively. The remainder of the edge values are computed analogously. Using the notation $\mathbf{F}^R = \mathbf{F}(m^R, \mathbf{u}^R)$ etc., the cell centered predicted values are

$$\mathbf{U}^{n+1/2} = \mathbf{U}^n - \frac{\tau}{2}\left[\frac{\mathbf{F}^R - \mathbf{F}^L}{\Delta r} + \frac{\mathbf{G}^T - \mathbf{G}^B}{\Delta z} - \mathbf{R}^n + \begin{pmatrix} r\nabla P_h^{n-1/2} \\ 0 \end{pmatrix}\right], \tag{3.2}$$

where $\tau = \tau^n$ is the time step, and $\nabla P_h^{n-1/2}$ is the approximation to the pressure gradient computed in the previous cycle (see the section on the pressure correction step below). The density is extracted from the predicted mass density using the truncating expression

$$\rho_{i+1/2,j+1/2}^{n+1/2} = \begin{cases} \dfrac{m_{i+1/2,j+1/2}^{n+1/2}}{r_{i+1/2}} & \text{if } m_{i+1/2,j+1/2}^{n+1/2} > 0, \\ 0 & \text{otherwise,} \end{cases} \tag{3.3a}$$

which guarantees non-negative values. The predicted velocities are then determined from

$$\mathbf{u}_{i+1/2,j+1/2}^{n+1/2} = \begin{cases} \dfrac{(m\mathbf{u})_{i+1/2,j+1/2}^{n+1/2}}{m_{i+1/2,j+1/2}^{n+1/2}} & \text{if } \rho_{i+1/2,j+1/2}^{n+1/2} > \varepsilon_\rho, \\ 0 & \text{otherwise,} \end{cases} \tag{3.3b}$$

where ε_ρ is a small positive number (in our computations we used $\varepsilon_\rho = 10^{-8}\rho_0$).

From the predicted values, numerical fluxes across each cell edge are computed. These fluxes are chosen to model the locally one-dimensional flow of inelastically colliding fluid particles and are based on the signs of the normal velocity on each side of the edge. To illustrate, consider the vertical edge $i, j+1/2$ between cells $C_{i-1/2,j+1/2}$ and $C_{i+1/2,j+1/2}$. Along this edge, left and right edge average values for $\mathbf{u}_h$ are computed using

$$\begin{aligned} \mathbf{u}_{i,j+1/2}^{R} &= \mathbf{u}_{i+1/2,j+1/2}^{n+1/2} - \frac{\Delta r_{i+1/2}}{2}(\mathbf{u}_r)_{i+1/2,j+1/2}^{n}, \\ \mathbf{u}_{i,j+1/2}^{L} &= \mathbf{u}_{i-1/2,j+1/2}^{n+1/2} + \frac{\Delta r_{i-1/2}}{2}(\mathbf{u}_r)_{i-1/2,j+1/2}^{n}, \end{aligned} \tag{3.4}$$

with similar expressions for the left and right values of m. The numerical flux across this edge is then given by

$$F_{i,j+1/2} = \begin{cases} \mathbf{F}_{i,j+1/2}^{L} + \mathbf{F}_{i,j+1/2}^{R} & \\ \quad \text{if } u_{i,j+1/2}^{L} \geqslant 0 \text{ and } u_{i,j+1/2}^{R} \leqslant 0, & \\ \mathbf{F}_{i,j+1/2}^{L} \quad \text{if } u_{i,j+1/2}^{L} > 0 \text{ and } u_{i,j+1/2}^{R} > 0, & \\ \mathbf{F}_{i,j+1/2}^{R} \quad \text{if } u_{i,j+1/2}^{L} < 0 \text{ and } u_{i,j+1/2}^{R} < 0, & \\ 0 \quad \text{otherwise.} & \end{cases} \tag{3.5}$$

The numerical fluxes $\mathbf{G}_{i+1/2,j}$ for the horizontal cell edges are determined by first computing top and bottom edge values analogous to the way the left and right values were computed in (3.4), and then using expressions analogous to (3.5) based on the signs of $v_{i+1/2,j}^{T}$ and $v_{i+1/2,j}^{B}$.

The momenta and mass density in each cell $C_{i+1/2,j+1/2}$ are then corrected using

$$\tilde{\mathbf{U}}^{n+1} = \mathbf{U}^n - \tau\left[\frac{\mathbf{F}_{i+1,j+1/2} - \mathbf{F}_{i,j+1/2}}{\Delta r_{i+1/2}} + \frac{\mathbf{G}_{i+1/2,j+1} - \mathbf{G}_{i+1/2,j}}{\Delta z_{j+1/2}} - \mathbf{R}^{n+1/2}\right],$$

where $\mathbf{R}^{n+1/2} = (0, -g(\tilde{m}^{n+1} + m^n)/2, 0)^t$. Finally, the density $\tilde{\rho}_{i+1/2,j+1/2}$ and velocities $\tilde{\mathbf{u}}_{i+1/2,j+1/2}$ are extracted from the corrected mass density and momenta using the procedure described in (3.3).

Redistribution of Density and Momenta

To compute the density redistribution we consider (2.8) in an equivalent more standard form, namely, find $H \geqslant 0$ such that

$$\begin{aligned} -\Delta H &= \tilde{\rho} - \rho_0, \quad \text{where } H > 0, \\ -\Delta H &\geqslant \tilde{\rho} - \rho_0, \quad \text{where } H = 0, \end{aligned} \tag{3.6a}$$

with boundary conditions

$$H=0 \quad \text{on } \Gamma_c, \qquad \frac{\partial H}{\partial \mathbf{n}}=0 \quad \text{on } \Gamma_a \cup \Gamma_w. \tag{3.6b}$$

After solving (3.6) the density is redistributed using

$$\bar{\rho}=\tilde{\rho}+\Delta H. \tag{3.7}$$

The discretization of the Laplacian is derived from a piecewise linear finite element discretization in each coordinate direction with the nodes located at the cell centers. This yields

$$\begin{aligned}(\mathbf{A}H_h)_{i+1/2,j+1/2} &\equiv (-\Delta_h H_h)_{i+1/2,j+1/2}(\tilde{d}V)_{i+1/2,j+1/2} \\ &= -\left[\frac{\tilde{r}_{i+1}(\delta_r H_h)_{i+1,j+1/2}-\tilde{r}_i(\delta_r H_h)_{i,j+1/2}}{\tilde{r}_{i+1/2}(\tilde{d}r)_{i+1/2}}\right. \\ &\quad \left.+\frac{(\delta_z H_h)_{i+1/2,j+1}-(\delta_z H_h)_{i+1/2,j}}{(\tilde{d}z)_{j+1/2}}\right](\tilde{d}V)_{i+1/2,j+1/2},\end{aligned} \tag{3.8a}$$

where Δ_h denotes a matrix approximation to the Laplacian, and

$$\tilde{r}_i=\frac{r_{i+1/2}+r_{i-1/2}}{2}, \tag{3.8b}$$

$$\tilde{r}_{i+1/2}=\frac{r_{i+3/2}+r_{i+1/2}+r_{i-1/2}}{3},$$

$$(\tilde{d}r)_{i+1/2}=\frac{r_{i+3/2}-r_{i-1/2}}{2}, \tag{3.8c}$$

$$(\tilde{d}z)_{j+1/2}=\frac{z_{j+3/2}-z_{j-1/2}}{2},$$

$$(\tilde{d}V)_{i+1/2,j+1/2}=\tilde{r}_{i+1/2}(\tilde{d}r)_{i+1/2}(\tilde{d}z)_{j+1/2}, \tag{3.8d}$$

$$(\delta_r H_h)_{i,j+1/2}=\frac{H_{i+1/2,j+1/2}-H_{i-1/2,j+1/2}}{r_{i+1/2}-r_{i-1/2}} \tag{3.8e}$$

$$(\delta_z H_h)_{i+1/2,j}=\frac{H_{i+1/2,j+1/2}-H_{i+1/2,j-1/2}}{z_{j+1/2}-z_{j-1/2}} \tag{3.8f}$$

The discrete Laplacian Δ_h is scaled by the (diagonal matrix of) local volumes $\tilde{d}V$ so that the matrix $\mathbf{A}$ is symmetric.

Dirichlet boundary conditions for H_h along Γ_c are imposed by simply setting $H_h=0$ in those cells adjacent to Γ_c. Neumann conditions are imposed by setting the corresponding difference of H_h to zero in (3.8) and by appropriately extending the grid variable definitions. For example, across Γ_a we set $(\delta_r H_h)_{0,j+1/2}=0$, and $r_{-1/2}=r_{1/2}$ in order to define $\tilde{r}_{1/2}$ and $(\tilde{d}r)_{1/2}$. The resulting matrix $\mathbf{A}$ remains symmetric and semi-definite and is positive definite if $\Gamma_c \neq \varnothing$.

Upon reordering the unknowns with a single index over all interior cells and cells adjacent to a Neumann boundary, the matrix $\mathbf{A}$ has a banded structure with five bands. By symmetry, only three bands need to be stored. The full discretization of (3.6a) is to find $H_h \geqslant 0$ ($H_l \geqslant 0$ for each l) such that

$$\begin{aligned}(\mathbf{A}H_h)_l &= (\tilde{\rho}_l-\rho_0)(\tilde{d}V)_l, \quad \text{where } H_l>0, \\ (\mathbf{A}H_h)_l &\geqslant (\tilde{\rho}_l-\rho_0)(\tilde{d}V)_l, \quad \text{where } H_l=0.\end{aligned} \tag{3.9}$$

This system is currently solved using a constrained conjugate gradient method with diagonal or incomplete Choleski preconditioning described in Appendix A. We remark that another successful iterative algorithm for (3.9) is the constrained successive over relaxation (SOR) method presented in [21]. However, numerical experiments have found the SOR procedure inferior to the method given in Appendix A, unless a nearly optimal relaxation parameter is used. For non-uniform grids this parameter can be determined only through numerical tests. Other possible approaches for solving (3.9) are discussed in [22–25].

For the momentum redistribution, we first recast (2.11) into self-adjoint form. Let $\mathbf{e} \equiv \bar{\rho}\bar{\mathbf{u}}-\tilde{\rho}\tilde{\mathbf{u}}$ and set

$$\bar{\mathbf{u}}=\begin{cases}(\mathbf{e}+\tilde{\rho}\tilde{\mathbf{u}})/\bar{\rho} & \text{if } \bar{\rho}>0, \\ \tilde{\mathbf{u}} & \text{if } \bar{\rho}=0,\end{cases} \tag{3.10}$$

$$\mathbf{q}=\begin{cases}H\mathbf{e}/\bar{\rho} & \text{if } \bar{\rho}>0, \\ \mathbf{0} & \text{if } \bar{\rho}=0,\end{cases}$$

$$\mathscr{F}=\begin{cases}H\tilde{\rho}\tilde{\mathbf{u}}/\bar{\rho} & \text{if } \bar{\rho}>0, \\ \mathbf{0} & \text{if } \bar{\rho}=0.\end{cases} \tag{3.11}$$

The case when $\bar{\rho}=0$ in (3.10) is consistent in the sense that if $0<\bar{\rho}<\rho_0$ in some region, then it can be shown that $\bar{\rho}=\tilde{\rho}$ and $H=\nabla H=\Delta H=0$ which implies, from (2.11), that $\bar{\mathbf{u}}=\tilde{\mathbf{u}}$. Furthermore, since $H=0$ when $0<\bar{\rho}<\rho_0$, $\mathbf{q}$ and $\mathscr{F}$ also vanish in the limiting case in (3.11). Substitution of (3.10) and (3.11) into (2.11) yields

$$-\Delta\mathbf{q}+\frac{\bar{\rho}\mathbf{q}}{H}=\Delta\mathscr{F} \quad \text{if } H>0, \tag{3.12a}$$

$$\mathbf{q}=0 \quad \text{if } H=0, \tag{3.12b}$$

where (3.12b) follows from the definition (3.11), since if $H=0$ then $\mathbf{q}\bar{\rho}=0$; thus if $\bar{\rho}>0$ then $\mathbf{q}=0$; otherwise, $\mathbf{q}=0$ by definition. Equations (3.12a) and (3.12b) are solved together with the boundary conditions

$$\mathbf{q}\cdot\mathbf{n}=0 \text{ and } \frac{\partial(\mathbf{q}-(\mathbf{q}\cdot\mathbf{n})\mathbf{n})}{\partial\mathbf{n}}=0 \quad \text{on } \Gamma_a \cup \Gamma_w. \tag{3.12c}$$

Note that since $H=0$ on Γ_c, $\mathbf{q}=0$ on Γ_c follows from (3.12b).

For the discretization of (3.12) we use the same discrete Laplacian for the interior nodes as described in (3.8). However, since $\mathbf{q}_{i+1/2,j+1/2}$ represents cell-averaged quantities, we do not impose zero normal values on cells adjacent to Γ_a or Γ_w. Instead, we add the unknowns $\mathbf{q}_{0,j+1/2}\cdot\mathbf{n}=(q_1)_{0,j+1/2}$ located at the nodes $(r_0, z_{j+1/2})$ along Γ_a, and then impose $(q_1)_{0,j+1/2}=0$ as the Dirichlet condition. Thus, the values $(q_1)_{1/2,j+1/2}$ are treated as interior unknowns. The corresponding terms in the discrete Laplacian matrix must be modified accordingly, and this modified Laplacian is denoted by $\tilde{\Delta}_h$. The analogous procedure is done along the wall boundaries Γ_w. The discrete function $\mathscr{F}_h$ is computed at each cell center using (3.11) with the condition $\bar{\rho}>0$ replaced by $\bar{\rho}_{i+1/2,j+1/2}>\varepsilon_\rho$ and $\bar{\rho}=0$ is replaced by $\bar{\rho}_{i+1/2,j+1/2}\leqslant\varepsilon_\rho$ (cf. (3.3b)).

The resulting pair of linear systems of equations is solved by a standard conjugate gradient method with diagonal preconditioning. We remark that particularly when H is small, these systems are very diagonally dominant, and the conjugate gradient method is very efficient. Furthermore, we iterate only over indices l, where $H_l>\varepsilon_H$ (in practice we use $\varepsilon_H=10^{-6}\rho_0$).

From $\mathbf{q}_h$, the determination of $\mathbf{e}_h$ follows from a discrete version of (2.11), namely,

$$\mathbf{e}_h=\tilde{\Delta}_h(\mathbf{q}_h+\mathscr{F}_h). \tag{3.13}$$

Finally we set

$$\bar{\mathbf{u}}_h=\begin{cases}\dfrac{\mathbf{e}_h+\bar{\rho}_h\tilde{\mathbf{u}}_h}{\bar{\rho}_h} & \text{if } \bar{\rho}_h>\varepsilon_\rho,\\ \tilde{\mathbf{u}}_h & \text{if } \bar{\rho}_h\leqslant\varepsilon_\rho.\end{cases} \tag{3.14}$$

Pressure Correction

The final step of the algorithm is the determination of the pressure from (2.13), (2.18) and the correction of the velocity (2.12) in the liquid region. The resulting discrete pressure is $P_h=P_h^{n+1/2}$. The numerical method described here will be in the context of the underwater bubble problem discussed at the end of the previous section. Let

$$\mathscr{W}=\Omega-(\bar{\mathscr{A}}\cup\bar{\mathscr{B}}\cup\bar{\mathscr{C}})=\mathrm{Int}(\mathscr{D}), \tag{3.15}$$

where the notation $\bar{\mathscr{S}}$ indicates the closure of the set $\mathscr{S}$. We approximate the solution to (2.13) by a continuous pressure P satisfying (2.18), with

$$\frac{\partial P}{\partial\mathbf{n}}=\frac{\rho_0}{\tau}\bar{\mathbf{u}}\cdot\mathbf{n} \quad \text{on } (\Gamma_a\cup\Gamma_w)\cap\bar{\mathscr{W}}, \tag{3.16a}$$

$$P=P_A+(z_s-z)\rho_0 g \quad \text{on } \Gamma_c\cap\bar{\mathscr{W}}, \tag{3.16b}$$

where z_s is the location of the free surface at "sea level." We can also consider the problem (2.13) as being solved in the region $\mathscr{W}$ with Dirichlet conditions for P specified on the boundaries of $\mathscr{A}$, $\mathscr{B}$, and $\mathscr{C}$.

We first describe an algorithm for evolving the air, bubble, and cavitation regions from time t^n to time t^{n+1} using the redistributed density $\bar{\rho}_h(=\rho_h^{n+1})$ obtained in the previous step. Again reordering indices with a single index over all cells, let

$$\mathscr{K}=\{l:\bar{\rho}_l<(1-\varepsilon_W)\rho_0\}$$

denote the set of indices of the non-liquid cells, where ε_W is a small positive number (in our computations, $\varepsilon_W=0.02$). Let

$$\mathscr{A}_h^n=\bigcup_{l\in I_A^n}\bar{C}_l \quad \text{and} \quad \mathscr{B}_h^n=\bigcup_{l\in I_B^n}\bar{C}_l$$

denote the discrete air and bubble regions from the previous step. Index sets I_A and I_B for these regions at the new time step are initialized as

$$I_A^{(0)}=I_A^n\cap\mathscr{K} \quad \text{and} \quad I_B^{(0)}=I_B^n\cap\mathscr{K}.$$

These sets are then iterated using

$$I_A^{(i)}=\left\{l\in\mathscr{K}:\bar{C}_l\cap\left(\bigcup_{j\in I_A^{(i-1)}}\bar{C}_j\right)\neq\varnothing\right\} \tag{3.17a}$$

$$I_B^{(i)}=\left\{l\in\mathscr{K}-I_A^{(i)}:\bar{C}_l\cap\left(\bigcup_{j\in I_B^{(i-1)}}\bar{C}_j\right)\neq\varnothing\right\} \tag{3.17b}$$

until $I_A^{(i)}=I_A^{(i-1)}\equiv I_A$ and $I_B^{(i)}=I_B^{(i-1)}\equiv I_B$. Each pass of (3.17a) turns all non-liquid cells, which are adjacent to the air region, into air cells. Thus, bubble or cavitation cells can "vent" into the air. All non-liquid cells, which have not been marked as air cells and are adjacent to a bubble cell, become bubble cells by (3.17b). Thus, cavitation cells can be merged into the bubble. Finally, the remainder of non-liquid cells which are neither air nor bubble are defined to be cavitation cells; that is,

$$I_C=\mathscr{K}-(I_A\cup I_B).$$

The new non-liquid regions are given by

$$\mathscr{A}_h=\bigcup_{l\in I_A}\bar{C}_l, \qquad \mathscr{B}_h=\bigcup_{l\in I_B}\bar{C}_l, \qquad \mathscr{C}_h=\bigcup_{l\in I_C}\bar{C}_l. \tag{3.18}$$

We remark that the above algorithm can be extended to include the cases when air entrapped bubbles are formed ($\mathscr{A}_h$ becomes disjoint), or independent multiple bubbles are formed ($\mathscr{B}_h$ becomes disjoint). A detailed description of

application featuring these events were presented in [26].

Analogous to (3.15) the discretization of $\mathscr{W}$ is given by

$$\mathscr{W}_h = \Omega - (\mathscr{A}_h \cup \mathscr{B}_h \cup \mathscr{C}_h).$$

We refer to the *Dirichlet boundary* of $\mathscr{W}_h$ as the boundary of $\mathscr{W}_h$ common to $\mathscr{A}_h$, $\mathscr{B}_h$, $\mathscr{C}_h$, or Γ_c. The discrete bubble volume needed to determine P_B from (2.17) is given by

$$(V_B)_h = \sum_{l \in I_B} (1 - \bar{\rho}_l/\rho_0)(\tilde{dV})_l.$$

The following spaces are used for our finite element discretization of (2.13), (2.18), and (3.16):

$\mathscr{V}_h = \{\phi_h : \phi_h$ is continuous in Ω and bilinear on each cell $C \in \Omega\}$,

$\mathscr{V}_h^\circ = \{\phi_h \in \mathscr{V}_h : \phi_h \geq 0$ in Ω, $\phi_h = 0$ along all Dirichlet boundaries of $\mathscr{W}_h$, and $\phi_h = 0$ in each cell $C \notin \mathscr{W}_h\}$,

$\mathscr{U}_h^0 = \{\mathbf{u}_h = (u_1, u_2) : \mathbf{u}_h$ is piecewise constant on each cell in $\Omega\}$,

$\mathscr{U}_h^\perp = \{\mathbf{u}_h = (u_1, u_2)$: on each cell $C \in \Omega$, u_1 is linear in z and constant in r, u_2 is linear in r and constant in z, and $\int_C \mathbf{u}_h = \mathbf{0}\}$.

Our finite element formulation of (2.13), (2.18), (3.16) is: find $\psi_h \in \mathscr{V}_h^\circ$ such that

$$(\nabla\psi_h, \nabla\phi_h) \geq \frac{\rho_0}{\tau}(\bar{\mathbf{u}}_h + (\mathbf{u}_h^\perp)^n, \nabla\phi_h) - (\nabla Q_h, \nabla\phi_h) \tag{3.19}$$

is satisfied for each $\phi_h \in \mathscr{V}_h^\circ$, where $Q_h \in \mathscr{V}_h$ satisfies (2.18) and (3.16b) with $\mathscr{A}$, $\mathscr{B}$, and $\mathscr{C}$ replaced by $\mathscr{A}_h$, $\mathscr{B}_h$, and $\mathscr{C}_h$, respectively, and $Q_h = P_C$ in $\mathscr{W}_h$. In (3.19) the inner product $(\cdot, \cdot)$ denotes integration over Ω (or, equivalently, over $\mathscr{W}_h$, since ϕ_h has support in $\mathscr{W}_h$). Once ψ_h is determined from (3.19), the discrete pressure $P_h \in \mathscr{V}_h$, approximating the solution to (2.13), (2.18), (3.16), is given by

$$P_h = \psi_h + Q_h. \tag{3.20}$$

Given $\mathbf{u}_h \in \mathscr{U}_h^1 \equiv \mathscr{U}_h^0 \oplus \mathscr{U}_h^\perp$, the discrete divergence of $\mathbf{u}_h$ is defined at the vertex point $(r_i, z_j) \equiv \mathbf{x}_l$, using the "weak" formula

$$(\nabla_h \cdot \mathbf{u}_h)_l = \frac{-(\mathbf{u}_h, \nabla\phi_h^l)}{(\phi_h^l, 1)}, \tag{3.21}$$

where $\phi_h^l \in \mathscr{V}_h$ satisfies $\phi_h^l(\mathbf{x}_l) = 1$, and $\phi_h^l = 0$ at all other vertex points. Noting that $\nabla P_h^{n+1/2} = \nabla P_h = (\nabla P_h)^0 +$ (3.19)–(3.21) that the "corrected velocity"

$$\mathbf{u}_h^* = \bar{\mathbf{u}}_h + (\mathbf{u}_h^\perp)^n - \frac{\tau}{\rho_0}\nabla P_h^{n+1/2} = \mathbf{u}_h^{n+1} + (\mathbf{u}_h^\perp)^{n+1} \tag{3.22}$$

satisfies the discrete analogue of (2.10) in $\mathscr{W}_h$.

Note that if we neglect the term $(\nabla P_h)^\perp$ and simply correct the velocity $\bar{\mathbf{u}}_h \in \mathscr{U}_h^0$ using

$$\mathbf{u}_h^* = \bar{\mathbf{u}}_h - \frac{\tau}{\rho_0}(\nabla P_h)^0, \tag{3.23}$$

then $\mathbf{u}_h^*$ cannot be ensured to satisfy (2.10) in the discrete sense. As a consequence, even if the velocity and density remain unchanged during the other steps of the algorithm, the pressure and, hence, the velocity will not remain unchanged after successive pressure correction steps using (3.19), (3.20), and (3.23). In other words, when $P_A = P_B = P_C$ and the inequality in (3.19) is satisfied with equality, (3.23) does not yield the projection of $\mathscr{U}_h^0$ onto its discretely divergence-free subspace. Numerically, this procedure can generate spurious pressure oscillations, particularly near the discrete bubble region. However, (3.19) (with equality), together with (3.20)–(3.22), defines a projection from $\mathscr{U}_h^1$ onto its discretely divergence-free subspace when $P_A = P_B = P_C$ and eliminates the spurious oscillations.

For computational simplicity, a matrix system of equations for values of P_h at all vertex points (except along Dirichlet boundaries) of Ω is considered. All equations corresponding to basis functions ϕ_h^l, where $l \in I_A \cup I_B \cup I_C$ are replaced by the equation $P_l = P_A$, P_B, or P_C, or equivalently, $\psi_l = 0$. The resulting matrix is symmetric and positive definite and has banded structure with nine bands (of which only five need to be stored by symmetry). In the current implementation we approximate the constrained problem by the unconstrained linear system in which the constraint $\phi_h \geq 0$ is removed from the definition of $\mathscr{V}_h^\circ$ and the inequality in (3.19) is replaced by equality. Wherever the resulting P falls below P_C it is set equal to P_C. This approximation is motivated by the fact that pressures below P_C rarely appeared in our computations for the examples presented in Section 4 and it is computationally more efficient to solve the unconstrained problem. The unconstrained linear system is solved using a conjugate gradient method with incomplete Choleski preconditioning with zero fill (see, e.g., [27]).

During the next cycle, $n \leftarrow n+1$, the approximation to ∇P used in the predictor (3.2) of the convection step is taken to be

$$(P_r^{n-1/2}, P_z^{n-1/2}) = (\nabla P_h^{n+1/2})^0.$$

The term $(\nabla P_h^{n+1/2})^{\perp}$ is not needed because $\int (\nabla P_h^{n+1/2})^{\perp} = 0$ on each cell and only first-order accuracy is required in the predictor (see, e.g., [19]).

Time Step Selection

The stability requirement for the time step τ^n is dictated by the Courant–Friedrichs–Lewy condition associated with the explicit convection step. This requirement is

$$\tau^n \|\mathbf{u}_h^n\|_h \leqslant \lambda < 1, \tag{3.24}$$

where

$$\|\mathbf{u}_h^n\|_h = \max_{i,j} \left(\frac{|u_{ij}^n|}{\Delta r_{i+1/2}} + \frac{|v_{ij}^n|}{\Delta z_{j+1/2}} \right). \tag{3.25}$$

In addition to (3.24) we also impose the condition that

$$\frac{(\tau^n)^2}{\rho_0} \|(\nabla P_h^{n-1/2})^0\|_h \leqslant \lambda < 1. \tag{3.26}$$

This additional restriction is imposed due to the inclusion of the pressure term in the convection step (3.2). Condition (3.26) restricts the time step primarily for bubble problems when the bubble radius is near an extremum, because in those cases the velocity is nearly zero.

Numerical errors due to time discretization are controlled using an adaptive time step selection based on the computed rate of energy loss. For classical flows the energy (2.20b) satisfies

$$\frac{dE}{dt} = 0. \tag{3.27}$$

Therefore,

$$T^n(\tau^{n-1}) = \frac{E^n - E^{n-1}}{\tau^{n-1}}$$

is an estimate of the local truncation error for Eq. (3.27). Given a bound δ on the local truncation error, the time step τ^n is taken to be

$$\frac{\tau^n}{\tau^{n-1}} = \begin{cases} \left(\dfrac{0.9\delta}{T^n}\right)^2 & \text{if } T^n \leqslant 0,\ |T^n| \geqslant \delta, \\ \left|\dfrac{0.9\delta}{T^n}\right| & \text{if } T^n \leqslant 0,\ |T^n| < 0.9\delta, \\ \left(\dfrac{0.9\delta}{2T^n}\right)^2 & \text{if } T^n > 0,\ |T^n| \geqslant \dfrac{\delta}{2}, \\ \dfrac{0.9\delta}{2T^n} & \text{if } T^n > 0,\ |T^n| < \dfrac{0.9\delta}{2}, \\ 1 & \text{otherwise,} \end{cases} \tag{3.28}$$

subject to $\frac{1}{2}\tau^{n-1} \leqslant \tau^n \leqslant 2\tau^{n-1}$ and $\tau^n \geqslant \tau_{\min}$, where $\tau_{\min}$ is a chosen lower bound on the time step. In the above, the value 0.9 is used as a "safety factor."

In the first case in (3.28) the energy is decreasing and the bound on the truncation error has been violated. Here the time step is decreased under the assumption that $T^{n+1}(\tau) = O(\tau^{1/2})$, reflecting a possible singularity in the solution of (3.27) due to liquid collisions. For example, for a one-dimensional collision of liquids at time t_c, the right-hand side of Eq. (3.27) should be replaced by a constant times $\delta(t - t_c)$, where $\delta(x)$ is the Dirac delta function, and thus E is discontinuous. When the truncation error is under the tolerance and the energy is decreasing as in the second case in (3.28), the time step is increased under the assumption that $T^{n+1}(\tau) = O(\tau)$. In the third and fourth cases the energy is increasing. As indicated in Section 2, this theoretically should not occur. The local truncation error tolerance is therefore reduced by a factor of two. A non-increasing energy is not ensured by our numerical algorithm (in particular the convection step) and computations have shown that some increases can occur, albeit rarely.

4. COMPUTATIONAL RESULTS

The first problem we consider is the face-on collision of two cylindrical masses of liquid in the absence of gravity. In Fig. 1 computed density and pressure contours are displayed at various times for such a problem. Initially both cylinders have radius $R = 1$, the upper cylinder has height $Z_1 = 1$ and is moving downward with velocity $\mathbf{u}_1 = -\mathbf{k}$, and the lower cylinder has height $Z_2 = 2$ and is moving upward with velocity $\mathbf{u}_2 = 0.5\mathbf{k}$. Under the assumptions that the liquid is incompressible, the collision is inelastic, and momentum is conserved, the exact energy loss at the moment of impact can be calculated analytically. Thus, this problem represents an important benchmark for our algorithm.

In general, let there be two regions in which $\rho = \rho_0$, denoted by $\mathscr{D}_1$ and $\mathscr{D}_2$, which collide at some instant $t = t_0$. At this instant, $\partial\mathscr{D}_1 \cap \partial\mathscr{D}_2 = \Gamma \neq \varnothing$, and an impulse $-\nabla I$ is transmitted to the liquid, such that

$$\lim_{t \downarrow t_0} \mathbf{u}(\mathbf{x}, t) = \lim_{t \uparrow t_0} \mathbf{u}(\mathbf{x}, t) - \frac{1}{\rho_0} \nabla I$$

is divergence-free in $\mathscr{D}_1 \cup \mathscr{D}_2$. Therefore, I satisfies the equation

$$\Delta I = -\rho_0 (\mathbf{u}_1 - \mathbf{u}_2) \cdot \mathbf{n} \delta_\Gamma, \tag{4.1a}$$

where δ_Γ is a Dirac measure on Γ and the unit normal $\mathbf{n}$

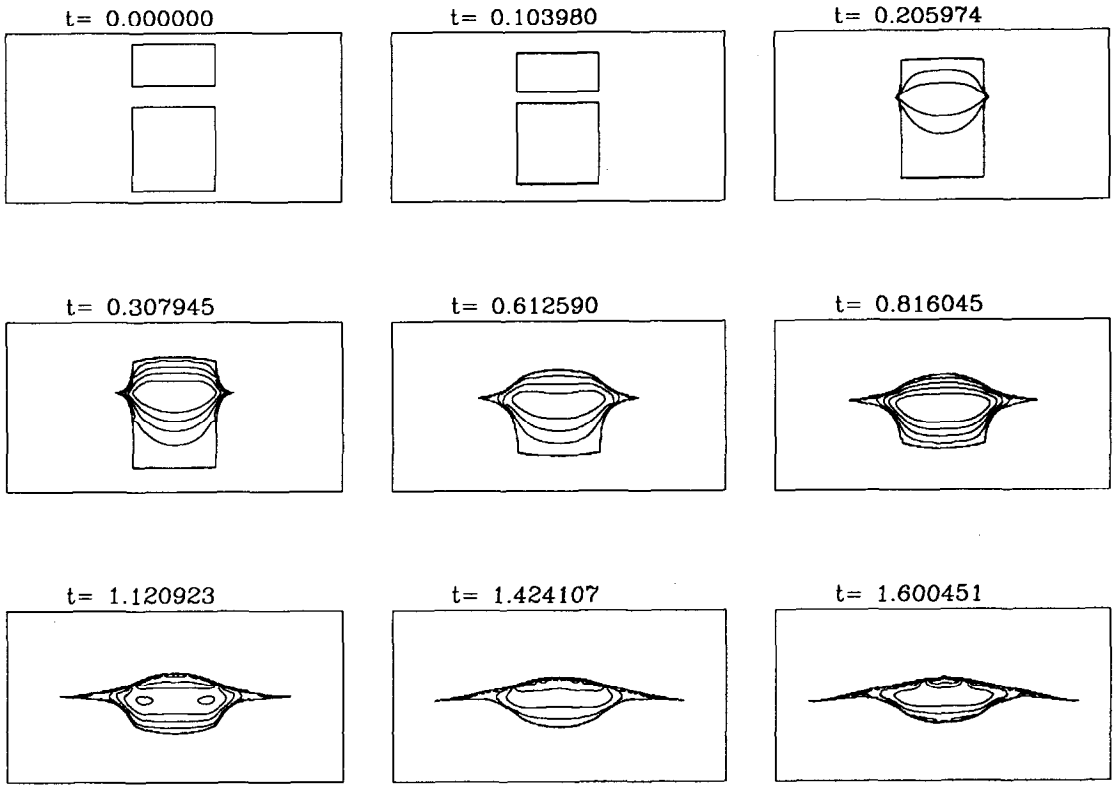

FIG. 1. Computed density and pressure contours for the evolution of two colliding cylinders of liquid. The computational grid was composed of 128 by 128 cells with $\Delta r = \Delta z = \frac{1}{32}$. The outline of the liquid region is displayed by contours of density in the range $0.9\rho_0 \leqslant \rho \leqslant 0.96\rho_0$.

points from region $\mathscr{D}_1$ into region $\mathscr{D}_2$. Boundary conditions for (4.1a) are

$$I = 0 \qquad \text{on } \partial\mathscr{D}, \tag{4.1b}$$

where $\mathscr{D}$ is the closure of $\mathscr{D}_1 \cup \mathscr{D}_2$. The energy lost in the collision is given by

$$\frac{1}{2\rho_0}\int_{\mathscr{D}} (\nabla I)^2 \, d\mathbf{x} = \frac{1}{2}\int_{\Gamma} I(\mathbf{u}_1 - \mathbf{u}_2)\cdot \mathbf{n} \, dS. \tag{4.2}$$

For the case in which the colliding cylinders have radii $R_1 = R_2 = R$ and heights Z_1 and Z_2, (4.1) can be solved using a separation of variables technique. In Appendix B it is shown that the energy loss expressed as a fraction of the kinetic energy of motion relative to the center of mass is

$$\mathscr{F} = \frac{4R(Z_1+Z_2)}{Z_1 Z_2} \sum_{n=1}^{\infty} \frac{1}{\mu_n^3}\left[\coth\frac{\mu_n Z_1}{R} + \coth\frac{\mu_n Z_2}{R}\right]^{-1}. \tag{4.3}$$

Here μ_n is the nth positive root of the Bessel function J_0.

For the initial configuration used in Fig. 1, the corresponding energy loss fraction is $\mathscr{F} = 24.087\%$. The computed energies, $E_h(t)$, on successively refined grids, where $h = \Delta r = \Delta z = \frac{1}{4}, \frac{1}{8}, \frac{1}{16}, \frac{1}{32}$, are displayed in Fig. 2, together with the exact energy $E_0(t)$. (These values are scaled so that $E_h(0) = 1$.) The time steps used in these calculations were determined using $\lambda = 0.4$ in (3.24) and (3.26), and the adaptive strategy described in (3.28) with $\delta = 3.2h$, $\tau_{\min} = 0.032h$, and $\tau_{\max} = 1000\tau_{\min}$. Table I lists the L_1 norm energy errors

$$\mathscr{E}(h) \equiv \|E_0 - E_h\| = \int_0^1 |E_0(t) - E_h(t)| \, dt,$$

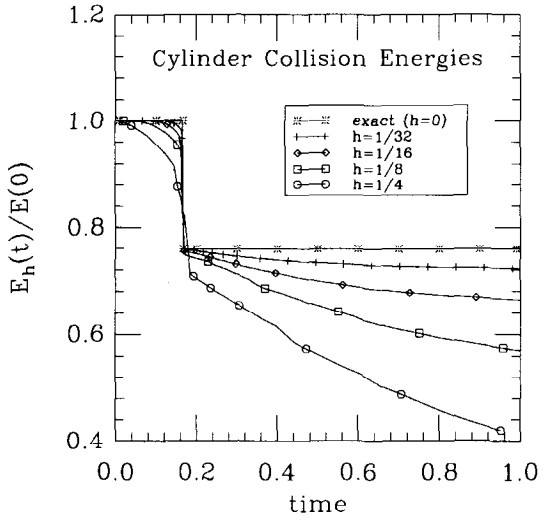

FIG. 2. Comparison of the computed time histories of the energy for the problem of Fig. 1 on various grids to the exact energy after the collision.

TABLE I

Errors and Rates of Convergence for Computations of the Collision of Two Cylinders of Water (cf. Fig. 1, 2)

h	$\mathscr{E}(h)$	$\alpha_{\mathscr{E}}(2h, h)$
$\frac{1}{4}$	0.187613	
$\frac{1}{8}$	0.098873	0.924
$\frac{1}{16}$	0.052656	0.909
$\frac{1}{32}$	0.021815	1.271

together with the rates of convergence

$$\alpha_{\mathscr{E}}(h_1, h_2) = \frac{\log(\mathscr{E}(h_1)/\mathscr{E}(h_2))}{\log(h_1/h_2)}.$$

The average rate of convergence for this problem is $\alpha_{\mathscr{E}}(\frac{1}{4}, \frac{1}{32}) = 1.035$, indicating that $\mathscr{E}(h) \approx O(h)$, which is optimal in the sense that it matches the rate of convergence in the square of the energy norm (4.2) for a finite element approximation to I satisfying (4.1) using bilinear elements.

Our next benchmark problem is the motion of a spherically symmetric adiabatic bubble in an infinite liquid region without the effects of gravity. Initially, the bubble is taken at its minimum radius $R(0) = R_{\min}$ and the liquid region is assumed to be at rest, so that $(dR/dt)(0) = 0$. The subsequent motion of such a bubble is governed by the equation (cf. [13])

$$R\frac{d^2R}{dt^2} + \frac{3}{2}\left(\frac{dR}{dt}\right)^2 = \frac{1}{\rho_0}\left(P_B(0)\left(\frac{R_{\min}}{R}\right)^{3\gamma} - P_\infty\right), \quad (4.4)$$

where $R = R(t)$ is the bubble radius at time t and P_∞ is the pressure at infinity. The initial bubble pressure is determined from an integration of (4.4) which yields

$$P_B(0) = P_\infty(1-\gamma)(1-a^3)/(1-a^{3(1-\gamma)}),$$

where a is the ratio of maximum to minimum bubble radii, $a = R_{\max}/R_{\min}$. For this study we selected $\gamma = 1.3$, $R_{\min} = 1$, $R_{\max} = 10$, $P_\infty = 10$, and $\rho_0 = 0.031081$. The numerical integration of (4.4) with the above values yields the "exact" (numerically converged to a tolerance of 10^{-6}) period $T = 1.0684$.

TABLE II

Computational Results for the Spherically Symmetric Bubble Problem

h	L	τ_{avg}	$R_{h,\max}$	$\alpha_{\mathscr{R}}(2h, h)$	T_h	$\alpha_{\mathscr{T}}(2h, h)$
1.0	106	2.04e-3	9.339		0.9748	
0.5	201	1.14e-3	9.643	0.888	1.0170	0.865
0.25	401	5.40e-4	9.814	0.941	1.0415	0.934

The computational grids used to study this problem consisted of a region of uniform cells, $\Delta r = \Delta z = h$, in the region $r < 12$, $|z - z_c| < 12$, where z_c is the z location of the center of the bubble. Outside this region the cells are stretched in the r direction using $\Delta r_{i+1/2} \approx 2^h \Delta r_{i-1/2}$ under the restriction that $\Delta r_{i+1/2} \leqslant 40h$, with identical stretching in the z direction on the top and bottom of the uniform grid region. The boundary condition $P = P_\infty$ is imposed along $r = R_R = L$, and $|z - z_c| = L$ (i.e., $z_c - Z_B = Z_T - z_c = L$). In order to demonstrate convergence of the method the value L was increased and the average time step τ_{avg} decreased as $h \to 0$. The adaptive time step strategy with parameters $\tau_{\max} = 100\tau_{\min} = 0.04h$, and tolerances $\delta = 0.2$, 0.15, and 0.10 for $h = 1.0$, 0.5, and 0.25, respectively, were selected so that τ_{avg} was decreased at approximately the same rate as h.

Table II summarizes the results of these calculations. The computed convergence rates $\alpha_{\mathscr{R}}$ and $\alpha_{\mathscr{T}}$ for the error in the maximum radius, $|R_{\max} - R_{h,\max}|$, and the error in the period, $|T - T_h|$, are indicative of first-order convergence, which is the best that can be expected since discontinuities in the density across free surfaces are "captured" by our algorithm.

The final example considered is the evolution of an underwater bubble in the absence of gravity, located in the vicinity of a solid wall at the bottom of the domain. With the exception of a solid wall boundary located at $Z_B = z_c - 10$, the initial conditions and grids used in the computations are the same as for the spherical bubble approximation described above.

The computed bubble evolution is displayed in Fig. 3 using the fine ($h = 0.25$) grid. The bubble retains a nearly spherical shape as it expands to a maximum volume at time $t = 0.61$. At the maximum, the radius of a sphere with the same volume is 9.81. During the contraction a high pressure region forms above the bubble ($t = 1.12$), causing the formation of a water jet which impacts the solid wall ($t = 1.21$) after which the bubble changes topology and forms a torus. In fact, shortly after the bubble attains its minimum volume at $t = 1.25$, it splits into two distinct torroidal bubbles between $t = 1.26$ and $t = 1.30$, and they recombine at

TABLE III

Summary of Computational Results for a Bubble in the Proximity of a Wall

h	$R_{h,\max}$	T_h	$T_{h,I}$	$U_{h,\max}$
1.0	9.367	1.155	1.149	5.959
0.5	9.651	1.218	1.192	6.859
0.25	9.810	1.252	1.211	7.530
↓	↓	↓	↓	↓
0.0	9.97	1.29	1.23	8.20

Note. The arrows indicate first-order extrapolation from the $h = 0.5$ and $h = 0.25$ computed values.

$t \approx 1.40$. The computed pressure contours and bubble shapes agree qualitatively with the results of Blake, Taib, and Doherty [6], using a boundary integral method, with the assumption that the bubble is a cavitation bubble with constant vapor pressure. However, they were unable to carry their computations past the time of "jet breakthrough," an event which has no special consequences for our algorithm.

Table III lists some quantitative results for solutions of this problem on the three computational grids. In this table the bubble "period" T_h is the time that the minimum bubble volume is attained, $T_{h,1}$ is the time that the water jet impacts

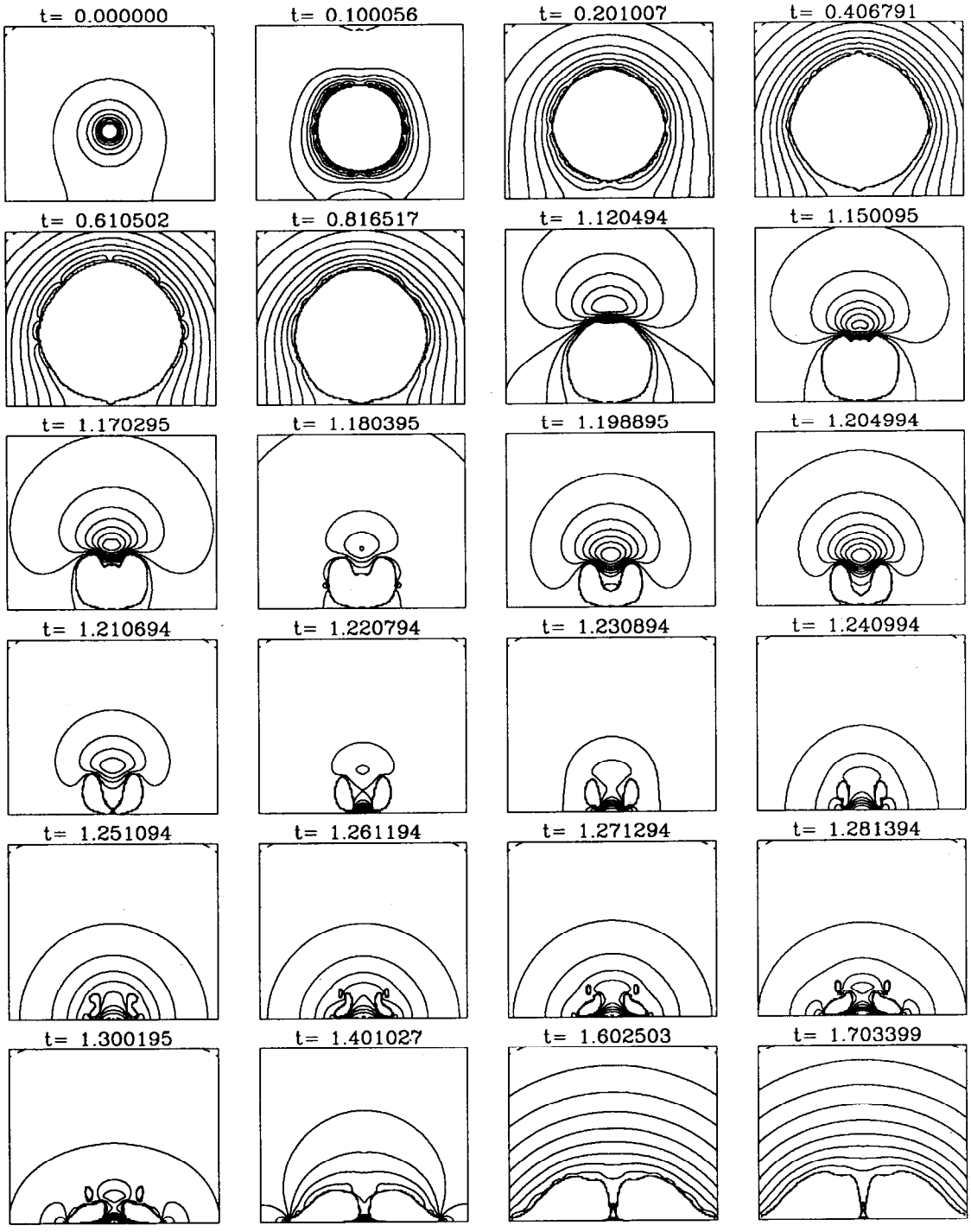

FIG. 3. Computed pressure and density contours for the evolution of a bubble near a solid bottom wall with gravity forces neglected.

the wall, and $U_{h,\max}$ is the scaled maximum water jet speed ($U_{h,\max} = \max_n |v^n_{\text{jet}}| ((P_\infty - P_v)/\rho_0)^{-1/2}$). The "jet speed," v^n_{jet}, is the velocity of the water cell along the axis and adjacent to the bubble, and P_v is the "vapor" pressure (which we have taken to be the bubble pressure at its maximum volume). Values for the bottom row of this table were obtained by extrapolating the corresponding $h = 0.5$ and $h = 0.25$ grid results assuming a first-order rate of convergence. Comparing these values with Table II, it can be inferred that although the maximum bubble radius is not significantly affected by the wall, the bubble period is increased by approximately 21%. Furthermore, the jet impacts the wall a time $0.0465T$ before the minimum volume is attained. The values listed in the final column indicate a rate of convergence of only 0.43 for $U_{h,\max}$. Since this maximum speed is attained before the jet impacts the wall, we expect that this rate is not due to a temporal singularity in the solution, but rather to an under-resolution of the jet on the coarsest grid. Thus, the true asymptotic rate will not be attained until the jet is sufficiently resolved. However, the extrapolated value of $U_{\max} = 8.2$ can be compared to a value of 8.6 reported in [6] using the constant vapor pressure model mentioned above, and a value of 7.6 determined experimentally in [28] for spark induced bubbles generated in free fall.

Figure 4 shows a comparison of the computed energies for the $h = 0.25$ bubble computations with and without the wall boundary. In the case when no wall is present the energy losses are due entirely to numerical dissipation. Figure 4 shows this dissipation to be greatest when Rayleigh–Taylor instability can be expected. Rayleigh–Taylor instability can occur when $P_B > P_\infty$ which comprises only 8.6% of the total time of the computation (from $t = 0$ to $t = 1.6$). During this time 63% of the energy loss occurred, despite the fact that the minimum time step was being selected by the adaptive time stepping strategy. When the wall is present energy losses are expected both from numerical dissipation and from the water jet impacting the solid wall and subsequent formation of the annular bubble (cf. Fig. 3). This is confirmed by our calculations. The energy loss for the problem in which no wall is present is approximately 14%, while the total energy loss with the wall boundary is 28%. Thus there is a loss of about 14% due to the jet impingment in this problem.

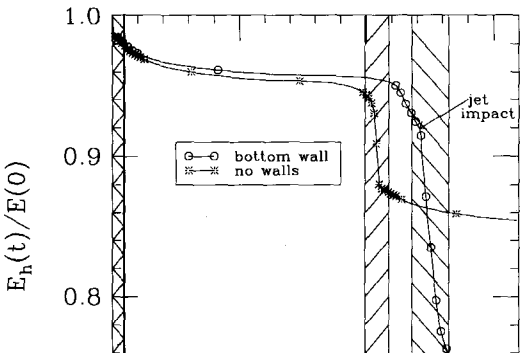

5. CONCLUDING REMARKS

In this paper a numerical algorithm for incompressible free surface problems has been presented. This algorithm provides a rational treatment of liquid on liquid or liquid on solid collisions based on the assumption that these collisions are inelastic. These collisions have an associated energy loss which can be attributed to turbulence. The algorithm also provides a robust method for treating problems where the free surfaces evolve into highly complex geometrical shapes.

The numerical examples were chosen primarily to demonstrate the applicability of the algorithm and its convergence properties. Numerical results of an inelastic collision of two liquid cylinders yielded energy losses which were converging at an optimal rate (with respect to uniform grid refinement) to the analytically determined value. For the problem involving the formation of a water jet and its subsequent impact against a solid wall, computed pressure contours and water jet shape agree well with the boundary integral method solutions found in [6]. The impact of the jet against the solid wall and the topological changes in the shape of the bubble(s) are events which cause a breakdown of classical boundary integral methods. That these events are of no special consequence in our formulation attests to the generality of our approach.

We remark that in the treatment of many free surface problems without surface tension, mathematical complications can arise. For example, in underwater bubble

(4b) Else if $\zeta < 0$ then enforce the constraint using P: set $X^\nu = X^{\nu-1} + \alpha P^\nu$, and $\zeta = 1$. For each k; if $X_k^\nu \leqslant 0$ and $X_k^{\nu-1} > 0$ then set $\zeta = -1$ and $P_k^\nu = -X_k^{\nu-1}/\alpha$. Next, if $\zeta < 0$ then recalculate α for the adjusted direction P^ν; i.e., compute AP^ν, $\beta_2 = P^\nu \cdot AP^\nu$, $\alpha_2 = R \cdot P^\nu$, and set $\alpha = \min(\alpha, \alpha_2/\beta_2)$.

(5) Calculate $X^\nu = X^{\nu-1} + \alpha P^\nu$.

(6a) (Calculate the error r_m after updating appropriate quantities) If $N_c = \tilde{N}_c$ then set $\zeta = -1$, $N_c = 0$, $X^\nu = \max(X^\nu, \mathbf{0})$, $R = F - AX^\nu$, $I^{\nu+1} = \{k : X_k^\nu > 0$ or $R_k > 0\}$, and $r_m = \max_{I^{\nu+1}} |R_k|/(\tilde{d}V)_k$.

(6b) Else if $N_c \geqslant \bar{N}_c$ then: set $R = F - AX^\nu$, $I^{\nu+1} = I^\nu$, and $r_m = \max_{I^{\nu+1}} |R_k|/(\tilde{d}V)_k$; if $r_m \leqslant \varepsilon$ then set $\zeta = -1$, $N_c = 0$, $X^\nu = \max(X^\nu, 0)$, $R = F - AX^\nu$, $I^{\nu+1} = \{k : X_k^\nu > 0$ or $R_k > 0\}$, and $r_m = \max_{I^{\nu+1}} |R_k|/(\tilde{d}V)_k$.

(6c) Else set $R = F - AX^\nu$, $I^{\nu+1} = \{k : X_k^\nu \geqslant 0$ or $R_k > 0\}$, and $r_m = \max_{I^{\nu+1}} |R_k|/(\tilde{d}V)_k$.

(7) (Convergence test) If $r_m \leqslant \varepsilon$ stop. If ν is larger than some fixed bound, print out a message and stop, else proceed with step (1) to start the next iteration.

In our hydrodynamic computations ε was chosen to be $10^{-3}\rho_0\tau$, where τ is the current time step. If convergence is obtained, then the resulting $\bar{\rho}$ given by the discrete version of (3.7) does not exceed $\rho_0 + \varepsilon$. The natural double indexing of the rectangular region was used in place of the single index k, making it easy to take advantage of the particular (sparse) form of A. If $\bar{N}_c$ and $\tilde{N}_c$ are set to infinity and step (2b) is deleted, it can be shown, using methods similar to those in [25, 30], that X^ν will converge to the solution of (A.1). In particular, the recalculation of α in step (4b) gives a positive lower bound on the decrease in the energy $\frac{1}{2}X \cdot AX - F \cdot X$ for DP steepest descent steps if a subsequence of X^ν were to converge to some $\tilde{X}$ not the solution of (A.1).

APPENDIX B: DERIVATION OF (4.3)

For the face-on collision of two coaxial liquid cylinders with equal radii R, consider a cylindrical coordinate system with the axis aligned with that of the liquid cylinders and such that $z = 0$ contains the impact surface Γ. On Γ, $(\mathbf{u}_1 - \mathbf{u}_2) \cdot \mathbf{n} = u_1 + u_2$, where $u_i = |\mathbf{u}_i|$ $(i = 1, 2)$ are constants. Setting

$$I(r, z) = \rho_0 R(u_1 + u_2)\, \mathscr{I}(r, z)$$

in (4.1), we find that $\mathscr{I}(r, z)$ satisfies

$$L(\mathscr{I}) \equiv \frac{1}{r}(r\mathscr{I}_r)_r + \mathscr{I}_{zz} = -\frac{1}{R}\delta(z) \qquad \text{in} \quad D = (0, R) \times (-Z_2, Z_1), \tag{B.1a}$$

with

$$\begin{aligned} &\mathscr{I}(r, Z_1) = \mathscr{I}(r, -Z_2) = 0 && \text{for} \quad 0 \leqslant r \leqslant R, \\ &\mathscr{I}(R, z) = 0 && \text{for} \quad -Z_2 \leqslant z \leqslant Z_1. \end{aligned} \tag{B.1b}$$

In the above, $\delta(z)$ is the standard Dirac measure on $z = 0$.

The energy loss in the collision given by (4.2) can be written as

$$\Delta E = \pi R \rho_0 (u_1 + u_2)^2 \int_0^R r\mathscr{I}(r, 0)\, dr.$$

Before impact the velocity of the center of mass is $[(Z_2 u_2 - Z_1 u_1)/(Z_1 + Z_2)]\mathbf{k}$ and the kinetic energy of the motion relative to the center of mass is given by

$$E_{\text{cm}} = \frac{\pi R^2 \rho_0 (u_1 + u_2)^2 Z_1 Z_2}{2(Z_1 + Z_2)}.$$

Hence,

$$\mathscr{F} \equiv \frac{\Delta E}{E_{\text{cm}}} = 4R\left(\frac{Z_1 + Z_2}{Z_1 Z_2}\right)\frac{1}{2R^2}\int_0^r r\mathscr{I}(r, 0)\, dr. \tag{B.2}$$

We seek a continuous solution to (B.1) of the form

$$\mathscr{I}(r, z) = \begin{cases} \mathscr{I}^{(1)}(r, z) & \text{for } (r, z) \in D_1 = [0, R] \times (0, Z_1] \\ \mathscr{I}^{(2)}(r, z) & \text{for } (r, z) \in D_2 = [0, R] \times [-Z_2, 0), \end{cases} \tag{B.3a}$$

where $\mathscr{I}^{(i)}$ are solutions of $L(\mathscr{I}^{(i)}) = 0$ satisfying conditions corresponding to (B.1b) on $\partial D_i \cap \partial D$ and

$$\begin{aligned} &\lim_{\varepsilon \downarrow 0} [\mathscr{I}^{(2)}(r, -\varepsilon) - \mathscr{I}^{(1)}(r, \varepsilon)] = 0 && \text{for} \quad 0 \leqslant r \leqslant R, \\ &\lim_{\varepsilon \downarrow 0} [\mathscr{I}_z^{(2)}(r, -\varepsilon) - \mathscr{I}_z^{(1)}(r, \varepsilon)] = \frac{1}{R} && \text{for} \quad 0 \leqslant r < R. \end{aligned} \tag{B.3b}$$

Using a standard separation of variables assumption in each subdomain D_i, we seek solutions of the form $\mathscr{I}^{(i)}(r, z) = \mathscr{R}(r)\, \mathscr{Z}(z)$, where $\mathscr{R}$ and $\mathscr{Z}$ satisfy

$$r\mathscr{R}'' + \mathscr{R}' + \lambda r \mathscr{R} = 0, \qquad \mathscr{Z}'' - \lambda \mathscr{Z} = 0,$$

respectively, and λ is constant. Assuming that $\mathscr{I}^{(i)}$ (and hence $\mathscr{R}$) is finite at $r = 0$ and vanishes at $r = R$, we conclude that $\mathscr{R}(r) = KJ_0(\mu_n r/R)$ and $\lambda = (\mu_n/R)^2$, where K is a constant, J_0 is the Bessel function of order zero, and μ_n is the nth positive root of $J_0(r) = 0$. Imposing $\mathscr{I}^{(1)}(r, Z_1) = \mathscr{I}^{(2)}(r, -Z_2) = 0$ and the first condition in (B.3b), we obtain the formal expressions

$$\mathscr{I}^{(i)}(r, z) = \sum_{n=1}^{\infty} C_n \frac{\sinh[\mu_n(Z_i + (-1)^i z)/R]}{\sinh(\mu_n Z_i/R)} J_0(\mu_n r/R) \tag{B.4a}$$

in D_i for $i=1, 2$, where the constants C_n, $n=1, 2, \ldots$, are determined by the second condition in (B.3b). Using the convergent expansion (see, e.g., [31])

$$\frac{}{R} = \frac{}{R} \sum_{n=1} \kappa_n J_0(\mu_n r/K) \qquad \text{for} \quad 0 \leqslant r < K,$$

where $\kappa_n = \beta_n^{-1} \int_0^1 \eta J_0(\mu_n \eta)\, d\eta$ and $\beta_n = [J_0'(\mu_n)]^2/2$ (note $\kappa_n = 2/(\mu_n J_1(\mu_n))$, cf. [32]); we find from the term-by-term differentiation of (B.4a) that

$$C_n = \frac{\kappa_n}{\mu_n} [\coth(\mu_n Z_1/R) + \coth(\mu_n Z_2/R)]^{-1}. \quad \text{(B.4b)}$$

To justify this formal construction, we note that $\mu_n \sim O(n)$ and $|\kappa_n| \sim O(n^{-1/2})$ as $n \to \infty$. Thus the series given in (B.4) is absolutely and uniformly convergent on $\bar{D}_i$ and $\mathscr{I}^{(i)}$ is continuous on $\bar{D}_i$. Furthermore, since each term in the series is harmonic in the interior of D_i, it follows by Harnack's theorem that $\mathscr{I}^{(i)}$ is also harmonic in the interior of D_i.

We have from (B.3) and the continuity of $\mathscr{I}^{(i)}$ on $\bar{D}_i$ that

$$\mathscr{I}(r, 0) = \sum_{n=1}^{\infty} C_n J_0(\mu_n r/R)$$

and

$$\frac{1}{2R^2} \int_0^R r \mathscr{I}(r, 0)\, dr = \frac{1}{2} \sum_{n=1}^{\infty} C_n \int_0^1 \eta J_0(\mu_n \eta)\, d\eta$$
$$= \sum_{n=1}^{\infty} C_n \kappa_n \beta_n / 2. \quad \text{(B.5)}$$

Since $\mu_n^2 \kappa_n^2 \beta_n = 2$, (B.2), (B.4b), and (B.5) imply (4.3).

ACKNOWLEDGMENT

We are grateful to Dianne P. O'Leary for helpful comments on solving quadratic programming problems.

REFERENCES

1. J. C. W. Rogers, Naval Ordnance Laboratory Report NSWC TR 75-43, 1975 (unpublished).
2. J. C. W. Rogers, "Incompressible Flows as a System of Conservation Laws with a Constraint," Seminaires IRIA Analyse et Contrôle de Systèmes, May 1978, p. 141.
3. J. C. W. Rogers, "An Algorithm for Predicting the Evolution of the Underwater Explosion Bubble," final report on Contract No. N60921-83-M-5807, March 1984 (unpublished).
4. J. C. W. Rogers, W. G. Szymczak, A. E. Berger, and J. M. Solomon, "Numerical Solution of Hydrodynamic Free Boundary Problems," in *Free Boundary Problems, Proceedings, Conference on Free Boundary Problems—Numerical Methods and Optimal Control, July 9–19, 1989,*
5. A. H. Van Tuyl and J. P. Collins, Naval Surface Weapons Center Report NSWC TR 84-314, July 1985 (unpublished).
6. J. R. Blake, B. B. Taib, and G. Doherty, *Fluid Mech.* **170**, 479 (1986).
7. J. P. Best and J. R. Blake, "Transient Inviscid Bubble Dynamics," ICIAM 91, Washington, DC, July 8–12, 1991.
8. G. L. Chahine, T. O. Perdue, and C. B. Tucker, Tracor Hydronautics Technical Report 86029-1, April 1988 (unpublished).
9. F. H. Harlow and J. E. Welch, *Phys. Fluids* **8**, 2182 (1970).
10. C. W. Hirt and B. D. Nichols, *J. Comput. Phys.* **39**, 201 (1981).
11. T. A. Reitter, R. W. Rosinsky, D. J. Steinberg, R. E. Tipton, and H. I. Zimmerman, Lawrence Livermore National Laboratory Report UCID-21175, Livermore, CA, August 28, 1987 (unpublished).
12. H. M. Sternberg and W. A. Walker, *Phys. Fluids* **14**, 1869 (1971).
13. R. H. Cole, *Underwater Explosions*, (Princeton Univ. Press, Princeton, NJ, 1948), p. 273.
14. J. C. W. Rogers, in *Free Boundary Problems, Vol. I, Proceedings, Seminar, Pavia, Sept.–Oct. 1979*), edited by E. Magenes (Istituto Nazionale di Alta Matematica, Rome, 1980), p. 333.
15. R. Courant and D. Hilbert, *Methods of Mathematical Physics. Vol. II. Partial Differential Equations* (Interscience, New York, 1962), p. 77.
16. J. C. W. Rogers, "Stability, Energy Conservation, and Turbulence for Water Waves," Seminaires IRIA Analyse et Contrôle de Systèmes, May 1978, p. 163.
17. J. B. Bell, P. Colella, and H. M. Glaz, *J. Comput. Phys.* **85**, 257 (1989).
18. J. B. Bell, J. M. Solomon, and W. G. Szymczak, "A Second-Order Projection Method for the Incompressible Navier–Stokes Equations on Quadrilateral Grids," AIAA 9th Computational Fluid Dynamics Conference, Buffalo, NY, June 13, 1989.
19. S. F. Davis, *SIAM J. Sci. Statist. Comput.* **9**, 445 (1988).
20. A. Harten, *J. Comput. Phys.* **49**, 357 (1983).
21. O. L. Mangasarian, *SIAM J. Numer. Anal.* **18**, 606 (1981).
22. Y. Lin and C. W. Cryer, *Appl. Math. Optim.* **13**, 1 (1985).
23. Y. Y. Lin and J.-S. Pang, *SIAM J. Control Optim.* **25**, 383 (1987).
24. P. Lötstedt, *BIT* **24**, 206 (1984).
25. D. P. O'Leary, *Linear Algebra Appl.* **34**, 371 (1980).
26. W. G. Szymczak, J. M. Solomon, A. E. Berger, and J. C. W. Rogers, "A Numerical Method Based on a Generalized Formulation of Hydrodynamic Free Surface Problems," AIAA 10th Computational Fluid Dynamics Conference in Honolulu, Hawaii, June 24, 1991.
27. G. H. Golub and C. F. Van Loan, *Matrix Computations*, Johns Hopkins Univ. Press, Baltimore, 1983.
28. D. C. Gibson, "Cavitation Adjacent to Plane Boundaries," in *Proceedings, 3rd Australian Conf. on Hydraulic and Fluid Mech., Inst. of Engs., Sydney, Aust., 1968*, p. 210.
29. J. C. W. Rogers, "Water Waves: Uniqueness and Continuous Dependence on the Data," Johns Hopkins Applied Physics Lab., 1977 (unpublished).
30. P. H. Calamai and J. J. Moré, *Math. Programming* **39**, 93 (1987).
31. G. N. Watson, *A Treatise on the Theory of Bessel Functions* (University Press, Cambridge, 1948), p. 581.
32. F. Bowman, *Introduction to Bessel Functions* (Dover, New York, 1958), pp. 108, 102, 93.